Antidiabetes and antioxidant potential of Schiff bases derived from 2-naphthaldehye and substituted aromatic amines: Synthesis, crystal structure, Hirshfeld surface analysis, computational, and *invitro* studies

Segun D. Oladipo [a,b,**], Robert C. Luckay [a,*], Kolawole A. Olofinsan [c], Vincent A. Obakachi [d], Sizwe J. Zamisa [e], Adesola A. Adeleke [b], Abosede A. Badeji [f], Segun A. Ogundare [b], Blassan P. George [c]

[a] *Department of Chemistry and Polymer Science, Stellenbosch University, Private Bag X1, Matieland, 7602, South Africa*
[b] *Department of Chemical Sciences, Olabisi Onabanjo University, P.M.B 2002, Ago-Iwoye, Nigeria*
[c] *Laser Research Centre, Faculty of Health Sciences, University of Johannesburg, P.O Box 17011, Doornfontein, 2028, South Africa*
[d] *Department of Pharmaceutical Chemistry, Discipline of Pharmaceutical Sciences, College of Health Sciences, University of Kwazulu-Natal, Durban, South Africa*
[e] *School of Chemistry and Physics, Westville Campus, University of KwaZulu-Natal, Private Bag X54001, Durban, 4000, South Africa*
[f] *Department of Chemical Sciences, Tai Solarin University of Education, Ijagun, Ogun State, Nigeria*

ABSTRACT

Three Schiff bases were synthesised by the condensation reaction between 2-napthaldehyde and aromatic amines to afford *(E)-N*-mesityl-1-(naphthalen-2-yl)methanimine (**L1**), *(E)-N*-(2,6-dime-thylphenyl)-1-(naphthalen-2-yl)methanimine (**L2**) and *(E)-N*-(2,6-diisopropylphenyl)-1-(naph-thalen-2-yl)methanimine (**L3**). The synthesised compounds were characterised using UV–visible, NMR (^{13}C & ^{1}H), and Fourier transform infrared spectroscopic methods while their purity was ascertained by elemental analysis. Structural analysis revealed that the naphthalene ring is almost coplanar with the imine functional group as evident by C1–C10–C11–N1 torsion angles of 176.4 (2)° and 179.4(1)° in **L2** and **L3**, respectively. Of all the various intermolecular contacts, H···H interactions contributed mostly towards the Hirshfeld surfaces of both **L2** (58.7 %) and **L3** (69.7 %). Quantum chemical descriptors of **L1** - **L3** were determined using Density Functional Theory (DFT) and the results obtained showed that the energy band gap (ΔE) for **L1**, **L2** and **L3** are 3.872, 4.023 and 4.004 eV respectively. The antidiabetic potential of the three compounds were studied using α-amylase and α-glucosidase assay. Compound **L1** showed very promising antidiabetic activities with IC$_{50}$ values of 58.85 μg/mL and 57.60 μg/mL while the reference drug (Acarbose) had 405.84 μg/mL and 35.69 μg/mL for α-amylase and α-glucosidase respectively. *In-silico* studies showed that **L1** docking score as well as binding energies are higher than that of acarbose, which are recognized inhibitors of α-amylase together with α-glucosidase. Further insight from the RMSF, RMSD and RoG analysis predicted that, throughout the simulation **L1** showcased evident influence on the structural stability of α-amylase. The antioxidant potential of the compounds was carried out using nitric oxide (NO), ferric reducing ability power (FRAP) and 2,2-diphenyl-1-

---

* Corresponding author.
** Corresponding author. Department of Chemistry and Polymer Science, Stellenbosch University, Private Bag X1, Matieland 7602, South Africa.
E-mail addresses: segun.oladipo@oouagoiwoye.edu.ng (S.D. Oladipo), rcluckay@sun.ac.za (R.C. Luckay).

picrylhydrazyl (DPPH) assays. The compounds exhibited good to fairly antioxidant properties with **L1** as well as **L3** having IC_{50} values of 70.91 and 91.21 µg/mL respectively for NO scavenging activities assay, which comparatively outshined acarbose (reference drug) with IC_{50} value of 109.95 µg/mL. Pharmacology and pharmacokinetics approximations of **L1** – **L3** showed minimal violation of Lipinski's Ro5 and this projects them to be less toxic and orally bioavailable as potential templates for the design of therapeutics with antioxidant and antidiabetic activities.

1. Introduction

Diabetes mellitus (D.M.) is an endocrinological disorder [1] caused by high blood glucose in animals due to inappropriate secretion of insulin by pancreas in the body. In the 14th century, diabetes mellitus was referred to as black death [2]. It is probably the oldest disease known to man and till today still remains a global health concern [3]. By 2030, researchers are projecting that, about 438 million people might have diabetes in 70 % developing countries if not checked [2]. One of the strategies adopted to combat diabetes mellitus, is to inhibit pancreatic α-amylase and intestinal α-glucosidase (hydrolytic enzymes) which are liable for breaking down carbohydrate into glucose in the body [4]. This will reduce glucose in the blood due to the decrease in the uses of dietary carbohydrates as well as suppresses postprandial glycemia [5]. Current generation of antidiabetic drugs i.e., Acarbose effectively decrease the intestinal absorption of glucose in human body [6]. However, complications such as meteorism, farting, swelling of the abdomen, and perhaps diarrhoea pose as great limitations to their utilisation [7]. Hence, the need to search for new antidiabetic drugs with little or no side effect with excellent activity (see Scheme 1).

Also, searching for novel antioxidants with excellent properties are of great importance due to their usefulness in slowing down aging, shielding biomolecules from oxidation and fortifying immune system against adverse effect of oxidation stress [8–10]. Reactive oxygen species (R.O.S.) i.e., superoxide radical ($O_2^{\bullet-}$) hydroxyl radical ($OH^{\bullet}$), hydrogen peroxide (H_2O_2), are the main cause of oxidative stress [11]. Though at low concentration, R.O.S. has beneficial roles such as defending the body against infectious agents, aid number of cellular signalling systems and induction of mitogenic response [12]. However, at high concentration, R.O.S. damages structures of the cells such as nucleic acids, proteins, membranes, lipids, among others, resulting in cardiovascular, neurodegenerative and cancerous inflammation diseases [13].

Schiff bases together with their metal complexes have been reported for their myriad biological applications [14–16]. They have been utilized as antibacterial [14], antioxidant [17], antituberculosis [18], antidiabetes [19], anticancer [20], among others [21]. The azomethine bond, also known as imine bond (−C═N) in Schiff bases are responsible for the crucial role during biological processes which it involves, and this facilitates their wide biological applications [22]. Here in, antidiabetics and antioxidant studies of Schiff bases prepared from 2-naphthaldehyde and aromatic amine is reported. The Schiff bases are designed in such a way to vary the alkyl groups. This would enable us to probe how electronic properties of organic compounds could affect their medicinal properties while we use theoretical approaches (DFT and Molecular docking) to support this assertion. All compounds are characterized by FT-IR, UV–Visible and N.M.R. spectroscopy. We also ran elemental analysis to confirm the purity of these compounds.

2. Experimental section

2.1. Materials

Solvents explored for this study were A.C.S. grade (purity ≥99.5 %) and used without further purification. Reagents used are 2,6-xylidine (99 %), 2,6-diisopropylphenylamine (97 %), mesidine (98 %) and 2-naphthaldehyde (98 %). All chemicals were sourced from Sigma-Aldrich.

2.2. Instrumentation

Bruker Avance[III] 400 MHz spectrometer were used to analyze ^1H and ^{13}C NMR spectra of **L1** – **L3** at 25 °C. Deuterated chloroform

$R^1 = R^2 = R^3 = Me : $ **L1**
$R^1 = R^2 = Me , R^3 = H : $ **L2**
$R^1 = R^2 = iPr , R^3 = H : $ **L3**
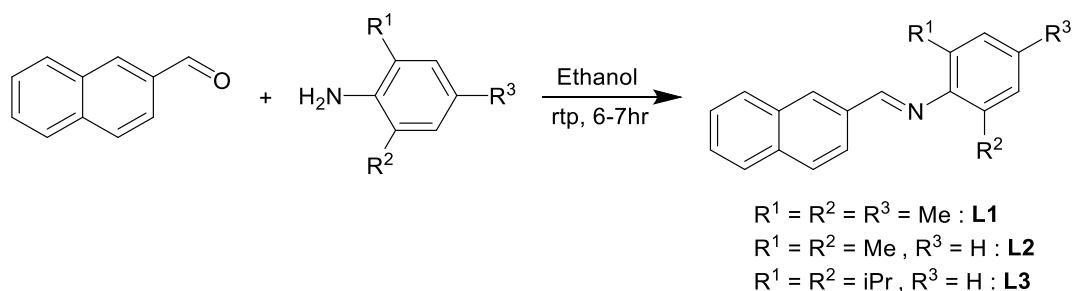
Scheme 1. Preparation of Schiff bases, **L1** – **L3**.

was used as a solvent to obtain the ^{1}H N.M.R. and ^{13}C N.M.R. data and signals at δ 7.26 and δ 77.00 ppm are referenced to residual CDCl$_3$. Vario elemental E.L. cube CHNS analyser was used for the elemental analysis and I.R. spectra were obtained on a PerkinElmer Universal A.T.R. spectrum 100 FT-IR spectrometer. Shimadzu UV–Vis–NIR spectrophotometer was used to process the electronic absorption spectra.

2.3. Synthesis of the Schiff bases

The compounds were prepared following a previously reported procedure [23,24]. 2-naphthaldehyde was added to a stirring ethanolic solution of the primary amine (2,6-xylidine, 2,6-diisopropylphenylamine, and mesidine) in a round bottom flask. Four droplets of glacial ethanoic acid were introduced into the mixture, and it was further stirred for 6–7 h at room temperature to afford off-yellow precipitates. The crude products were rinsed thoroughly with hexane to remove unreacted anilines, dried and kept in an air-tight desiccator for further work.

2.3.1. Synthesis of (E)-N-mesityl-1-(naphthalen-2-yl)methanimine

The reaction of 2-naphthaldehyde (0.8 g, 5 mmol) and mesidine (0.7 ml, 5 mmol) in 30 mL of ethanol furnished compound **L1** as off-yellow powder. Yield: 82 %, z g. M.p: 162–163 °C. ^{1}H N.M.R. (CDCl$_3$, 600 MHz): δ (ppm) 2.19 (s, 6H, CH$_3$-Ar), 2.33 (s, 3H, CH$_3$-Ar), 6.94 (s, 2H, Ar–H), 7.59 (m, 2H, J$_{H.H.}$ = 6, Ar–H), 7.93 (d, 1H, J$_{H.H.}$ = 12, Ar–H), 7.97 (d, 2H, J$_{H.H.}$ = 12, Ar–H), 8.18 (s, 1H, Ar–H), 8.25 (d, 1H, J$_{H.H.}$ = 6, Ar–H), 8.39 (s, 1H, CH═N). ^{13}C N.M.R. (CDCl$_3$, 150 MHz) δ (ppm): 0.17.23, 19.73, 122.60, 125.62, 126.50, 127.62, 127.71, 127.73, 127.84, 129.84, 132.06, 134.06, 147.70, and 161.73. IR υ (cm^{-1}): 3079(w), 1649(s), 1573(s), 1375(s), 1219 (s), 726(m), 590(m). Anal. calcd for C$_{20}$H$_{19}$N: C, 87.87; H, 7.01; N, 5.12; Found: C, 87.99; H, 7.27; N, 5.37.

2.3.2. Synthesis of (E)-N-(2,6-dimethylphenyl)-1-(naphthalen-2-yl)methanimine

The reaction of 2-naphthaldehyde (0.8 g, 5 mmol) and 2,6-xylidine (0.6 ml, 5 mmol) in 30 mL of ethanol furnished compound **L2** as off-yellow powder. Yield: 87 %, z g. M.p: 174–175 °C. ^{1}H N.M.R. (CDCl$_3$, 600 MHz): δ (ppm) 2.22 (s, 6H, CH$_3$-Ar), 7.01 (t, 1H, J$_{H.H.}$ = 6, Ar–H), 7.12 (d, 2H, J$_{H.H.}$ = 6, Ar–H), 7.59 (m, 2H, J$_{H.H.}$ = 6, Ar–H), 7.94 (d, 1H, J$_{H.H.}$ = 6, Ar–H), 7.98 (q, 2H, J$_{H.H.}$ = 6, Ar–H), 8.19 (s, 1H, Ar–H), 8.26 (d, 1H, J$_{H.H.}$ = 6, Ar–H), 8.41 (s, 1H, CH═N). ^{13}C N.M.R. (CDCl$_3$, 150 MHz) δ (ppm): 18.46, 123.71, 123.84, 126.81, 127.30, 127.71, 128.10, 128.20, 128.82, 128.88, 131.07, 133.22, 133.90, 135.25, 151.38, 162.78. IR υ (cm^{-1}): 3057(w), 1632 (s), 1575(s), 1377(s), 1217(s), 732(m), 599(m). Anal. calcd for C$_{19}$H$_{17}$N: C, 87.99; H, 6.61; N, 5.40; Found: C, 88.09; H, 6.97; N, 5.47.

2.3.3. Synthesis of (E)-N-(2,6-diisopropylphenyl)-1-(naphthalen-2-yl)methanimine

The reaction of 2-naphthaldehyde (0.8 g, 5 mmol) and 2,6-diisopropylphenylamine (0.9 ml, 5 mmol) in 30 mL of ethanol furnished compound **L3** as off-yellow powder. Yield: 87 %, z g. M.p: 168–170 °C. ^{1}H NMR (CDCl$_3$, 600 MHz): δ (ppm) 1.22 (d, 12H, CH$_3$–CH), 3.06 (m, 2H, J$_{HH}$ = 6, CH$_3$–**CH**-Ar), 7.16 (t, 1H, J$_{HH}$ = 6, Ar–H), 7.22 (d, 2H, J$_{HH}$ = 6, Ar–H), 7.59 (m, 2H, J$_{HH}$ = 6, Ar–H), 7.94 (d, 1H, J$_{HH}$ = 12, Ar–H), 7.99 (t, 2H, J$_{HH}$ = 12, Ar–H), 8.20 (s, 1H, Ar–H), 8.25 (d, 1H, J$_{HH}$ = 12, Ar–H), 8.38 (s, 1H, CH═N). ^{13}C N.M.R.

Table 1

Summary of X-ray structure refinement parameters and crystal data collection for **L2** and **L3**.

Compound	L2	L3
Empirical formula	C$_{19}$H$_{17}$N	C$_{23}$H$_{25}$N
Formula weight	259.33	315.44
Temperature/K	296.15	296.15
Crystal system	Orthorhombic	Monoclinic
Space group	$P2_12_12_1$	$P2_1/n$
a/Å	7.0306(5)	13.5344(4)
b/Å	13.743(1)	11.4699(3)
c/Å	15.381(1)	13.7414(6)
α/°	90	90
β/°	90	119.150(1)
γ/°	90	90
Volume/Å^3	1486.2(2)	1863.0(1)
Z	4	4
ρ$_{calc}$g/cm^3	1.159	1.125
μ/mm^{-1}	0.067	0.064
F(000)	552.0	680.0
Crystal size/mm^3	0.18 × 0.14 × 0.08	0.28 × 0.22 × 0.18
2Θ range for data collection/°	7.028 to 56.526	4.912 to 56.496
Index ranges	−9 ≤ h ≤ 2, −18 ≤ k ≤ 17, −19 ≤ l ≤ 20	−15 ≤ h ≤ 17, −15 ≤ k ≤ 15, −18 ≤ l ≤ 16
Reflections collected	8741	20119
Independent reflections	3644 [R$_{int}$ = 0.0238, R$_{sigma}$ = 0.0244]	4582 [R$_{int}$ = 0.0244, R$_{sigma}$ = 0.0170]
Data/restraints/parameters	3644/0/183	4582/0/221
Goodness-of-fit on F^2	1.044	1.033
Final R indexes [I ≥ 2σ (I)]	R$_1$ = 0.0397, wR$_2$ = 0.1011	R$_1$ = 0.0457, wR$_2$ = 0.1237
Final R indexes [all data]	R$_1$ = 0.0493, wR$_2$ = 0.1086	R$_1$ = 0.0597, wR$_2$ = 0.1371
Largest diff. peak/hole/e Å^{-3}	0.12/-0.14	0.21/-0.14

(CDCl$_3$, 150 MHz) δ (ppm): 23.64, 28.14, 123.20, 123.83, 124.28, 126.84, 127.73, 128.11, 128.89, 131.11, 133.26, 133.87, 135.25, 137.80, 149.50, 162.20. IR υ (cm^{-1}): 3053(w), 1643(s), 1587(s), 1381(s), 1203(s), 743(m), 605(m). Anal. calcd for C$_{23}$H$_{25}$N: C, 87.57; H, 7.99; N, 4.44; Found: C, 87.78; H, 7.99; N, 4.71.

2.4. Crystal structure determination

Recrystallization of ethanolic solution of **L2** and **L3** affords a suitable single crystal utilized in this X-ray diffraction study. Bruker Smart APEXII diffractometer with Mo Kα radiation was used for the crystal evaluation and data collection. At different starting angles, reflections were collected, and these were indexed using *APEX*II program suite [25]. *SAINT* software was explored for data reduction [26] while *SADABS* multi-scan technique [27] was used for scaling and absorption corrections. *SHELXS* program and *SHELXL* program [28] were used to solve (using direct methods) and refine structures respectively. *OLEX2* software [29] was used in designing the graphics of the crystal structures. Non-hydrogen atoms were first refined isotropically and then by anisotropic refinement with the full-matrix least-squares method based on F^2 using *SHELXL* [28]. The refinement parameters and crystallographic data for **L2** and **L3** are given in Table 1.

2.5. In vitro antidiabetes studies

2.5.1. α-amylase enzyme inhibitory activity
Using a modified procedure presented by Ibitoye et al. [30], the inhibitory effect of ligands **L1 - L3** on α-amylase enzyme activity was evaluated. In a 20,000 μM buffer solution (mono/dibasic sodium phosphate salt, pH 6.8) with 5 U/mL pancreatic α-amylase, increasing doses (63–500 μg/mL) of the ligands or acarbose were incubated for 10 min at 37 °C. The solution was equilibrated further for 20 min at 37 °C after adding 200 μL of 10 mg/mL starch solution. 0.6 mL of DNSA before boiling at 100 °C in a water bath for 10 min. At 540 nm, the optical density of the coloured mixture formed was read in comparison to a control solution devoid of the inhibitors.

2.5.2. α-Glucosidase enzyme inhibitory activity
This activity of ligands **L1 - L3** on α-glucosidase enzyme was also elucidated using *p*-nitrophenol glucopyranoside (pNPG) as the substrate in a slightly modified method from the literature [31]. 0.4 mL of yeast α-glucosidase (1 U/mL) was added to 0.5 mL solution of **L1**-**L3** or acarbose, along with 500 μL of one hundred millimolar buffer solution (mono/dibasic sodium phosphate salt, pH 6.8), and the mixture was incubated at 37 °C for 15 min. The amount of yellow *p*-nitrophenol emitted from the substrate was then measured at 405 nm after adding 0.2 ml of pNPG (0.005 M).

2.6. In vitro antioxidant activity experiment

2.6.1. Nitric oxide (NO) scavenging capacity
This *in vitro* assay of the **L1 - L3** compounds was done via NO scavenging estimation. The Kurian et al. method [32] was employed in this assay. A 0.50 mL aliquot of various concentrations of **L1 - L3** or Trolox was equilibrated at 25 °C for 2 h with 10 mM sodium nitroprusside dispersed in pH 7.4 PBS. Griess reagent (0.20 mL) was added to the solution, before further equilibration at 25 °C for 5 min. Then, using a blank solution devoid of the test samples, the NO scavenging abilities of **L1 - L3** and the standard were read at 546 nm.

2.6.2. 2,2′-diphenyl-1-picrylhydrazyl (DPPH) mopping capacity
This assay was done by determining the capacity of the compounds to release electrons to purple-coloured DPPH free radical using Turkoglu et al. [33] previous protocol with minor modification. 400 μL aliquot of 63–500 μg/mL concentrations of the Schiff bases or Trolox and DPPH solution (300 μM) in methanol were maintained away from light for 30 min at ambient laboratory temperature. Then, absorbance was read at 516 nm against a control solution devoid of the samples or Trolox.

2.6.3. Ferric (Fe^{3+}) reducing power capacity
This property of the **L1 - L3** Schiff bases was evaluated using potassium ferricyanide K$_3$Fe(C.N.)$_6$ in accordance with Tan and Chan's method [34]. 300 μL of two hundred millimolar phosphate buffer was incubated with 500 μL solution of each **L1 - L3** or Trolox (63–500 μg/mL) and 500 μL of 1 % K$_3$Fe(CN)$_6$ solution at 50 °C for 25 min. Afterward, 0.4 mM of 0.1 g/mL TCA solution was added before dilution with 0.3 mL distilled water. The optical density of the resultant mixture was read at 700 nm after adding 0.2 mL FeCl$_3$ (0.1 %). From a standard curve made with gallic acid (y = 0.0243x - 0.0586; R^2 = 0.9852), the compounds' capacity to reduce ferric ion was estimated.

2.7. Computational method

2.7.1. DFT calculations
DFT Becke 3 Lee Yang Par (B3LYP) [35] and the 6–31 +G(d,p) basis set for all atoms were employed to optimize the synthesised compounds **L1 - L3** to produce the three-dimensional layout using Gaussian 16 module available on the Lengua cluster of the centre for high performance computing (CHPC), Cape Town, South Africa. The frontier molecular orbital (FMO) hypothesis was used to analyze

the compounds' chemical reactivity [36]. The part of the molecule with the lowest unoccupied and highest occupied molecular orbitals (LUMO and HOMO) is revealed by FMO studies.

2.7.2. Molecular docking procedure

This docking analysis was done to determine the compounds' affinity for certain carbohydrate-digesting enzymes. In this procedure, α-glucosidase [37] and α-amylase [38] 3D crystallographic structures with the identification codes 1B2Y and 3CTT, respectively, were downloaded from the Protein Data Bank which is an online database (accessed on May 14, 2023). The Chimera software (V.1.16) Dock prep tool's algorithm was employed to delete water molecules and non-protein chemical components that co-crystallized with the enzymes. Then, according to Wang et al. [39], an automated software added hydrogen atoms and gasteiger charges. Prior to 3D conversion and structural optimization with Avogadro software [40], ChemBioDraw Ultra 14.0 was used to create the 2D structures of **L1**, **L2**, and **L3** (Hanwell et al., 2012). The Schiff bases 3D structures were then independently loaded into UCSF Chimera application (V1.16) and prepared following the same steps as with the digestive enzymes. Each protein's catalytic pocket occupied by their co-crystallized inhibitors (acarbose for α-amylase & casuarine for α-glucosidase), was covered by the search volume while docking. Subsequently, BIOVIA Discovery Studio [41] was utilized to study the 2D interactions of the most stable ligand-protein complexes while their predicted binding energies were also recorded.

2.7.3. Molecular dynamic simulation

The AMBER force field's FF18SB variant [42] was utilized to describe the systems in the GPU style of the AMBER software (AMBER 18), which was used for molecular dynamic simulations. Using the General Amber Force Field (GAFF) and Restrained Electrostatic Potential (RESP) methods, ANTECHAMBER produced atomic partial charges for the ligands. To neutralize all systems, the Leap module of AMBER 18 permitted the inclusion of hydrogen atoms, as well as Na^+ and Cl^- counterions to α-Amylase. After that, the systems were implicitly suspended within an orthorhombic box made of TIP3P water molecules, with each atom being within 8 Å of any box edge [43]. After heating, an equilibration estimating 200 ps (minimization of 500,000 steps) of each system was conducted; the operating temperature was kept constant at 300 K. With an imposed restraint potential of 500 kcal/mol for both solutes, a preliminary minimization of 2500 steps was completed. The steepest descent method was used for 1000 steps, while conjugate slopes were used for 1500 steps. A further full minimization of 1000 steps was completed using the conjugate gradient algorithm without constraints. A molecular dynamic simulation with gradual heating from 0 K to 300 K was run for 5 ps (minimization of 2500 steps), keeping the systems' volume and atom count constant. The system solutes were imposed with a collision frequency of 1 ps and a potential harmonic constraint of 10 kcal/mol. The pressure and other elements were maintained constant, simulating an isobaric-isothermal ensemble. The Berendsen barostat [44] was used to maintain the system pressure at 1 bar. The SHAKE algorithm was used [45] to constrict hydrogen atom bonds over the course of the molecular dynamic simulation, which took more than 100 ns in total. Each simulation employed an SPFP precision model with a 2 fs step size [46]. The isobaric-isothermal ensemble (N.P.T.), randomized seeding, constant pressure of 1 bar maintained by the Berendsen barostat, pressure-coupling constant of 2 ps, temperature of 300 K, and Langevin thermostat with a collision frequency of 1 ps were all present in the simulations [47].

2.7.4. Binding free energy calculations of the complexes

The molecular Mechanics/Poisson-Boltzmann surface area approach (MM/PBSA) was used to compute the free binding energy to determine the compounds' binding affinity [48]. The binding free energy was averaged over 100,000 snapshots extracted from the 100 ns trajectory. The following equation can be used to express the free binding energy (ΔG) calculated using this method for each molecular species (complex, ligand, and receptor):

$$\Delta G_{bind} = G_{complex} - G_{receptor} - G_{ligand} \tag{1}$$

$$\Delta G_{bind} = E_{gas} + G_{sol} - TS \tag{2}$$

$$E_{gas} = E_{int} + E_{vdw} + E_{ele} \tag{3}$$

$$G_{sol} = G_{GB} + G_{SA} \tag{4}$$

$$G_{SA} = \gamma \, SASA \tag{5}$$

The E_{gas} stands for gas-phase energy, which is made up of the internal energy E_{int}, Coulomb energy E_{ele} and the van der Waals energies E_{vdw}. The FF14SB force field terms were used to estimate the E_{gas} directly. The energy contribution from the polar, $G_{G.B.}$ and non-polar, G states was used to compute the solvent-free energy, G_{sol}. Using a water probe radius of 1.4 Å, the non-polar solvation (S. A.) energy, $G_{S.A.}$, was calculated from the solvent-accessible surface area (SASA). While the contribution of the polar solvation, $G_{G.B.}$, was estimated by solving the G.B. equation, S and T represent the total entropy of the solute and temperature, respectively.

2.7.5. Post molecular dynamic analysis

The analysis of Radius of gyration (RoG), Root mean square fluctuation (RMSF) and the Root mean square deviation (RMSD) were done using CPPTRAJ module found in the AMBER 18 suit [49]. The Origin data analysis program was used to generate all average raw data visualizations [50].

3. Results and discussion

3.1. Synthesis

Compounds L1 - L3 were synthesised by introducing 2-naphthaldehyde into a vigorously stirred ethanolic solution containing aromatic amines (namely, 2,6-xylidine, 2,6-diisopropylphenylamine, and mesidine). Following this addition, 2 to 3 drops of glacial acetic acid were incorporated into the resulting solution, and the reaction was allowed to proceed for a duration of 6 h. A pale-yellow solid precipitate formed as a result, which was subsequently filtered and washed with dry hexane three times to eliminate any unreacted amines. The resulting products were left to air dry at room temperature overnight and were then securely stored in a dry vial placed inside a desiccator.

3.2. Spectroscopic studies

3.2.1. ^1H and ^{13}C NMR

The ^1H and ^{13}C NMR spectra for L1 to L3 were recorded in CDCl$_3$, and their peaks were assigned using 2D NMR techniques. In all compounds, the aliphatic proton signals fell within the range of 1.22–3.06 ppm. Specifically, the methyl proton signals for L1 were detected at 2.19 ppm and 2.33 ppm, whereas those for L2 and L3 were observed at 2.22 ppm and 1.22 ppm, respectively. Within the ^1H NMR spectra of L3, quintet peaks between 3.03 and 3.08 ppm were attributed to the methine protons (CH–CH$_3$) within the isopropyl group of L3. Additionally, signals between 6.94 and 8.26 ppm, primarily appearing as singlets, doublets, triplets, and quintets, were assigned to the aromatic protons found in the benzene and naphthalene rings. Distinct peaks at 8.39 ppm for L1, 8.41 ppm for L2, and 8.38 ppm for L3 were also identified in the ^1H NMR spectra, and these were attributed to the imine protons (—CH=N) within the compounds. In the ^{13}C NMR spectra, the imine carbon (—CH=N) resonated at 162 ppm, while the carbon atoms connecting the imine group to the benzene ring (—CH=N–C) appeared in the downfield region, specifically between 149 and 152 ppm. Other carbon signals, such as those from aromatic carbons, were observed within the range of 127–136 ppm, while aliphatic carbons exhibited signals around 18–29 ppm. See Fig. S1–S9 in supplementary information for the N.M.R. spectra.

3.2.2. FT-IR and UV–visible spectra of L1 – L3

The Fourier transform infrared spectra of L1 – L3 showcase the major diagnostic peaks. The vibrational frequency band corresponding to the imine (—CH=N) group is characterized by a sharp peak at approximately 1649–1632 cm^{-1}, consistent with previously reported findings in the literature [23,51]. Additionally, the Sp^3 C–H and Sp^2 C–H bands are observed around 2914–2954 cm^{-1} and 3079–3053 cm^{-1}, respectively. The bending vibrational band associated with ortho-substituted benzene in L1 – L3 is evident around 724–726 cm^{-1}, while peaks around 953–977 cm^{-1} can be assigned to the trans –CH=CH— absorption band, as reported by Kemp [52]. The UV–Visible spectra of L1 – L3 in dichloromethane solvent are provided in the supplementary material (Fig. S13). An intense absorption band appeared in the wavelength range of 235–240 nm, which can be attributed to the π→π* transition induced by the
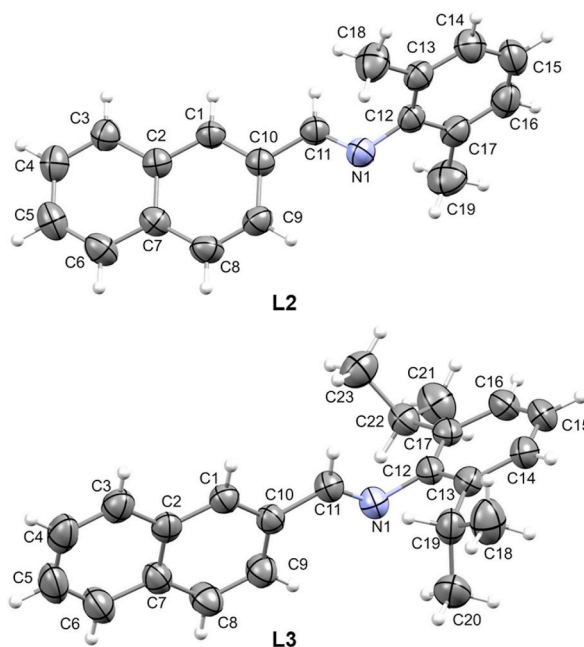

Fig. 1. Structures of L2 and L3 with thermal ellipsoids drawn at 50 % probability.

excitation of electrons within the aromatic ring. The second, less intense band, observed around 280–290 nm, is associated with the π→π* transition of the imine functional group, which results from the overlap of two shoulder bands [51].

3.3. Crystal structure analysis for L2 and L3

The crystal structures of **L2** and **L3** each contain one molecule in their respective asymmetric units as shown in Fig. 1. To best describe and compare the molecular conformation of **L2** and **L3**, C1–C10–C11–N1 and C11–N1–C12–C13 torsion angles were selected. The naphthalene ring is almost coplanar with the imine functional group as evident by C1–C10–C11–N1 torsion angles of 176.4(2)° and 179.4(1)° in **L2** and **L3**, respectively. The geometric orientation of the 2,6-disubstituted phenyl ring appears to be nearly orthogonal to the imine functional group with C11–N1–C12–C13 torsion angles of 73.7(2)° and 78.5(1)° in **L2** and **L3**, respectively. The broadening of the C1–C10–C11–N1 and C11–N1–C12–C13 torsion angles could be ascribed to the availability of sterically demanding iso-propyl substituents in **L3** relative to methyl substituents in **L2**. To the best of our knowledge, we are the first to report the crystal structures of *N*-(2-naphthylmethylene)-aniline Schiff bases since no hits of closely related compounds were obtained in the Cambridge Structural Database (C.S.D.; version 5.43, November 2022 update) [53]. However, the bond distances and angles in **L2** and **L3** were found to be comparable with those of *N*-(1-naphthylmethylene)-aniline Schiff bases (C.S.D. ref. codes: **DONVOU** [54] and **EXIPIL** [55]).

3.3.1. Analysis of intermolecular interactions in L2 and L3

Intermolecular interactions in the crystal packing of **L2** and **L3** are depicted in Fig. 2 while their geometric parameters are listed in Table 1. In **L2**, numerous intermolecular C–H … π interactions were observed in the crystal packing. For instance, the H1 and H8 hydrogen atoms of the naphthalene ring exhibits intermolecular C–H … π interactions with the naphthalene ($\pi_{naphthalene}$) and phenyl (π_{phenyl}) rings of two separate neighbouring molecules. The H11 hydrogen atom of the imine carbon forms C11–H11 … $\pi_{naphthalene}$ interactions with a naphthalene ring of the same neighbouring molecule as did the H1 hydrogen atom. Collectively, the C–H … π_{phenyl}
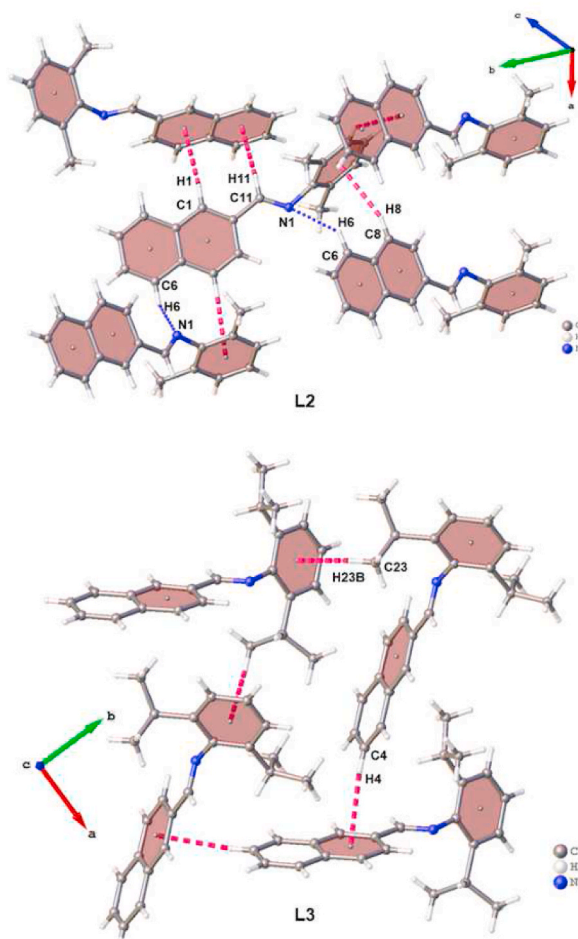

Fig. 2. Graphical representation of intermolecular C–H … π interactions (magenta-coloured dashed bonds) and C–H···N hydrogen bonds (blue-coloured dotted bonds) in the crystal packing of **L2** and **L3**.

and C–H … $\pi_{\text{naphthalene}}$ link together neighbouring molecules of **L2** to form chains that extend along the crystallographic *a* axis. These chain-like structures are linked by intermolecular C6–H6···N1 hydrogen bonds to form a two-dimensional supramolecular structure which propagates along the crystallographic *ab* plane. In **L3**, the *iso*-propyl group's H23B atom and the naphthalene ring's H4 atom participate in intermolecular C23–H23B … π_{phenyl} and C4–H4 … $\pi_{\text{naphthalene}}$ interactions, respectively. These interactions form a 2D supramolecular structure which extends along the crystallographic *ab* plane.

3.3.2. Hirshfeld surface analysis of L2 and L3

The Hirshfeld surface of a crystal is known to be the locations in which the electron density contribution from the molecule within the surface is equal to the contributions from all other molecules. The investigation of crystal structures and the arrangement of molecules offers valuable understanding into this particular phenomenon. The significance of Hirshfeld surface in the field of crystal engineering is paramount [56] as it facilitates the examination of data related to both weak and strong interactions within the crystal system. Fig. 3 depicts the Hirshfeld surfaces of **L2** and **L3** that have been mapped using the d_{norm} function including the 2D fingerprint plots of the various intermolecular contacts, were generated using *CrystalExplorer21* [57]. The Hirshfeld surface is visually encoded with the colours red, white, and blue, which correspond to the mapped d_{norm} values [58]. The presence of negative values in the d_{norm} distribution, as observed in the red regions, signifies that intermolecular distances are comparatively diminutive. The blue regions exhibit positive d_{norm} values, which signify an increased number of contacts. Conversely, the white regions display d_{norm} values of zero, indicating contact distances in relation to the van der Waals separation [59]. This section exclusively focuses on the discussion of short intermolecular contacts, as they are believed to play a crucial role in stabilising the crystal lattice. Of all the various intermolecular contacts, H···H contacts were found to contribute the most towards the Hirshfeld surfaces of both **L2** (58.7 %) and **L3** (69.7 %). The large contribution of H···H contacts in **L3** is attributed due to its higher hydrogen content (7.99 %) than that of **L2** (6.61 %). Reciprocal H···C contacts were attributed to intermolecular C–H … π interactions and they contributed 38.8 % and 29.0 % towards the Hirshfeld surface of **L2** and **L3**, respectively. Lastly, intermolecular C–H···N hydrogen bonds were reciprocal N···H contacts and they contribute 1.8 % and 0.7 % towards the Hirshfeld surface of **L2** and **L3**, respectively.

3.4. Quantum chemical descriptors

The calculated values for relevant quantum descriptors for **L1** – **L3** are given in Table 2 while their isodensity plots for crucial
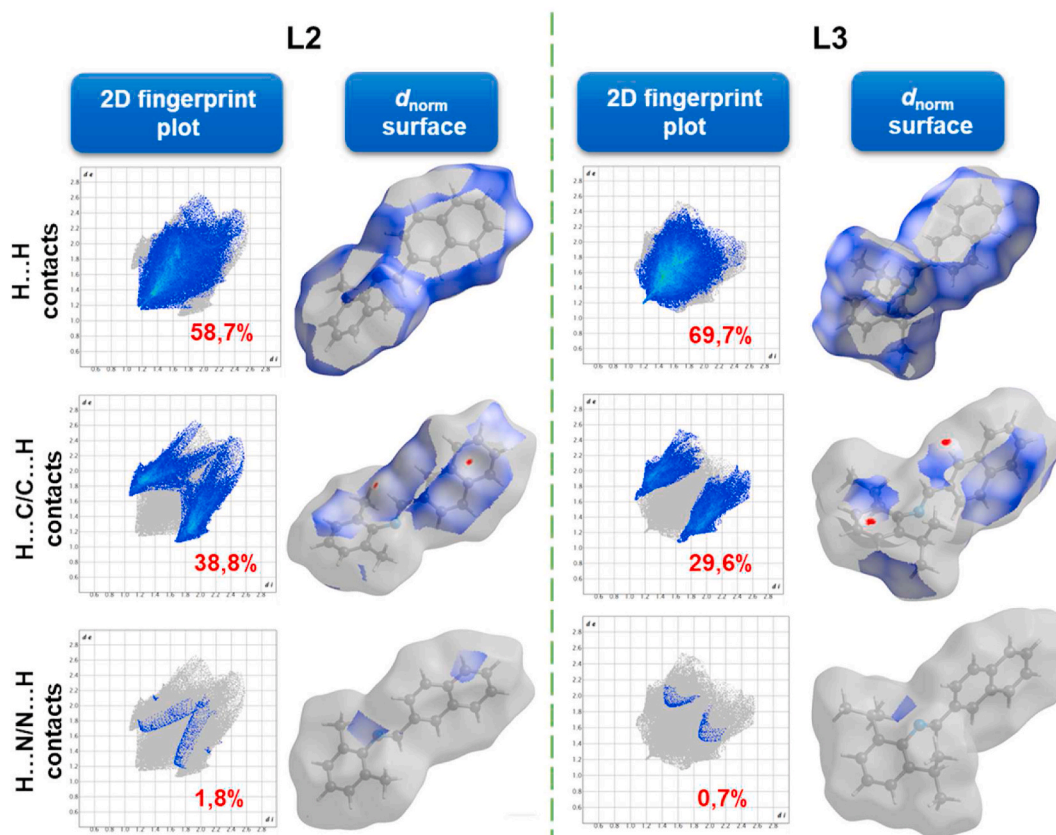

Fig. 3. d_{norm} property generated over the Hirshfeld surface and fingerprint plots of the intermolecular contacts with their contribution towards the Hirshfeld surface of **L2** and **L3**.

molecular orbitals are presented in Fig. 4. These quantum descriptor values offer valuable insights into the stability, reactivity, as well as selectivity of organic molecules. Specifically, E_{HOMO} values signify a compound's capacity to give out its most loosely bound electron to a suitable orbital of an acceptor molecule. The higher the E_{HOMO}, the better the electron-donating power of compounds and on the contrary the higher the L_{HOMO} the better the electron-accepting ability [60,61]. Among the studied compounds, it is likely that **L1**, which possesses an E_{HOMO} value of −5.769 eV, exhibits the highest electron-donating capability. The calculation of energy band gaps (ΔE) through the subtraction of E_{HOMO} from L_{HOMO} serves as a metric for assessing chemical reactivity and stability. It has been reported that a lower ΔE indicates a higher level of both stability and reactivity. Specifically, the calculated **ΔE** values for **L1**, **L2**, and **L3** are 3.872 eV, 4.023 eV, and 4.004 eV, respectively. Consequently, it can be inferred that **L1**, with its lower ΔE value, may possess greater reactivity and stability when compared to **L2** and **L3**.

The global softness (S) characterizes how easily the electron cloud of molecules can undergo deformation or polarization in response to small chemical perturbations. Among the compounds considered, **L1** exhibits the highest global softness at 0.258 eV^{-1}. This implies that the electron cloud of **L1** readily deforms or polarizes, rendering it more chemically active compared to **L2** and **L3**. Conversely, global hardness (η) is the inverse of global softness, indicating that higher global hardness values correspond to lower chemical reactivity. Examining Tables 2 and it becomes evident that **L2** possesses the highest global hardness value, suggesting it is likely the least reactive among the synthesised compounds. The electrophilic (ω) properties for **L1**, **L2**, and **L3** are determined to be 3.794, 3.861, and 3.875 eV, respectively. These values reveal that **L3** exhibits the highest electrophilic ability, while **L1** demonstrates the highest nucleophilic ability. Furthermore, the calculated ionization potential (I.P.) values reflect the nucleophilic properties of the synthesised compounds, while the electron affinity (E.A.) values indicate their ability to attract electrons. Notably, **L3** possess the highest electron affinity, while **L2** has the highest ionization potential.

3.5. Schiff bases L1 – L3 effects on carbohydrate digestive enzyme

3.5.1. α-Amylase inhibition

As displayed in Fig. 5, it is evident that the % α-amylase inhibitory activities increase with increasing concentration. While the percentage inhibition of both sample **L1** and sample **L2**, as well as Acarbose, was indistinguishable at 63 µg/mL, Table 3 reveals that sample **L1** exhibited the highest suppressive effect on the carbohydrate digestive enzyme, as indicated by its IC_{50} value of 58.85 µg/mL, which is significantly lower than that of Acarbose (405.84 µg/mL) and the other compounds (**L2** > 500 µg/mL; **L3** > 500 µg/mL).

3.5.2. α-Glucosidase inhibition

The results illustrating the inhibitory capacity of the Schiff bases on α-glucosidase are presented in Fig. 6. Among the synthesised samples, **L1** exhibited a significantly higher inhibitory effect at concentrations of 63–125 µg/mL. Furthermore, when comparing **L1**, **L2**, and acarbose, their percentage inhibition at 250 µg/mL did not exhibit statistically significant differences, however, at a concentration of 500 µg/mL, **L2** displayed significantly greater activity. Intrestingly, the IC_{50} values for these Schiff bases, as shown in Table 3, were higher compared to acarbose (IC_{50} = 35.67 µg/mL). More importantly, **L1** demonstrated the most potent enzyme inhibition amongst the compounds, with an IC_{50} value of 57.60 µg/mL. This suggests that **L1** holds promise as a potential template in the development of antidiabetic therapeutics.

3.6. Computational techniques

3.6.1. Molecular dynamic simulation

Molecular docking experiments were employed in order to anticipate the binding energies of compounds **L1** – **L3** and acarbose, which served as a reference drug. These studies were conducted with specific target enzymes, namely alpha-amylase and alpha-glucosidase. The binding energies obtained are summarized in Table 4, while comprehensive insights into the interactions between the receptors and ligands can be found in the supplementary material (Fig. S14–S18). Remarkably, among all the compounds tested, L1 exhibited the highest binding scores, surpassing even acarbose in terms of binding affinity. This finding is in excellent agreement with experimental results, where L1 demonstrated greater promise than the reference drug. To comprehend **L1**'s binding affinity and its potential as an anti-diabetic agent against α-amylase in comparison to acarbose, an extensive analysis involving molecular dynamic simulations (MDS) was carried out. This analysis focused on **L1**, which exhibited notable docking scores, and acarbose (the reference

Table 2
Quantum chemical descriptors of compounds **L1** - **L3**.

Parameters	L1	L2	L3
E_{HOMO} (eV)	−5.769	−5.953	−5.941
E_{LUMO} (eV)	−1.897	−1.930	−1.937
ΔE (eV)	3.872	4.023	4.004
η (eV)	1.936	2.012	2.002
S (eV^{-1})	0.258	0.249	0.250
IP (eV)	5.769	5.953	5.941
A (eV)	1.897	1.930	1.937
χ (eV)	−3.833	−3.941	−3.939
ω (eV)	3.794	3.861	3.875

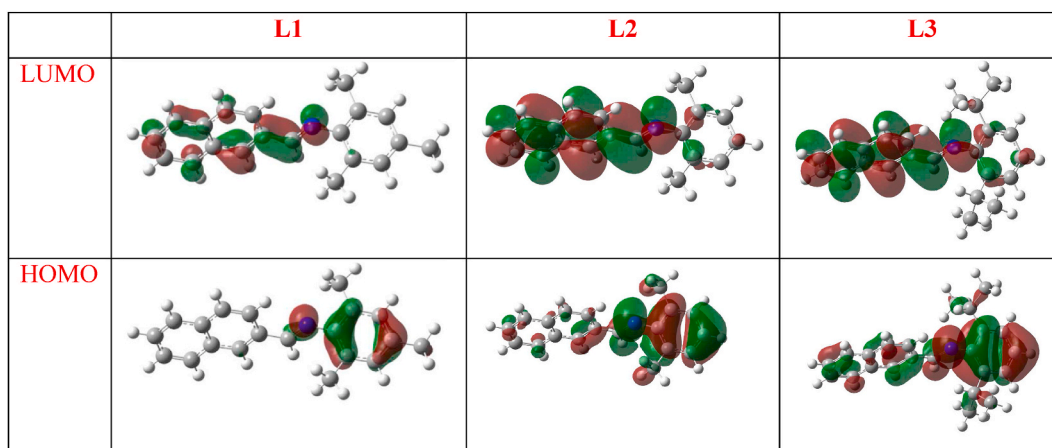|	**L1**	**L2**	**L3**
LUMO			
HOMO			

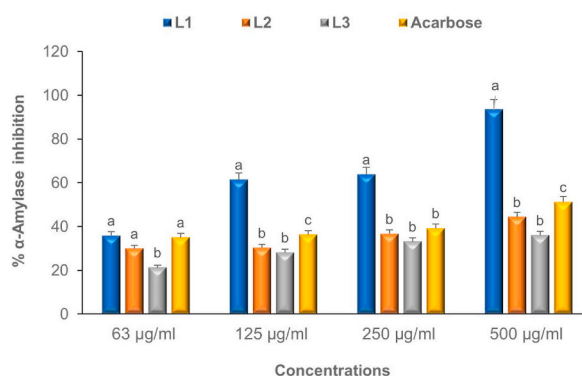**Fig. 4.** HOMO and LUMO plots for studied Schiff bases L1 – L3 at the SMD/B3LYP/6-31+G(d) level of theory.

Fig. 5. Effect of L1 – L3 synthesised Schiff bases on α-amylase enzyme inhibition. The mean activity ± standard deviation of each compound represented by bars at each concentration with different alphabets (a–c) are significantly different at $p < 0.05$.

Table 3
Antidiabetic potential of **L1** – **L3** at different concentration using α-glucosidase and α-amylase assays.

Compounds	α-Amylase (μg/mL)	α-Glucosidase (μg/mL)
L1	58.85	57. 60
L2	>500	147.42
L3	>500	206.02
Acarbose (Standard)	405.84	35.67

drug).

Molecular dynamics (M.D.) simulations are of great importance in this study because they encompass intricate molecular structural motions, enabling a comprehensive analysis of structural shades at specific protein sites. This includes identifying crucial binding regions (hot spots) and eliminating structural anomalies that may arise due to the conditions used in MD characterization, as emphasized in the work done by Hernández-Rodríguez et al. [62]. Moreover, MD simulations provide a robust foundation for improving the accuracy of free energy estimations related to interactions between proteins and ligands, a valuable complement to experimental procedures [62]. After conducting extensive 100 ns molecular dynamics (MD) simulations in our current study, we employed the molecular mechanics Poisson-Boltzmann surface area (MMPBSA) technique. The MMPBSA approach is highly regarded for its robustness and reliability in estimating binding free energies (ΔGbind) in various molecular recognition scenarios, with a notable example being the research conducted by Wang and colleagues in 2018 [63]. MMPBSA was employed in a meticulous examination of the interactions between molecules involving **L1** and α-Amylase, as well as the reference standard (acarbose). The outcome of these simulations, as shown in Table 5, showed the binding free energy score of **L1** complexes to be −22.627 kcalmol^{-1}, whereas the standard reference, acarbose, exhibited a binding free energy of −22.206 kcalmol^{-1}, determined through the integration of various energy components. This insightful analysis sheds light on the favourable binding affinity of **L1** compared to the reference standard acarbose, providing valuable molecular-level insights into their interactions with α-Amylase.
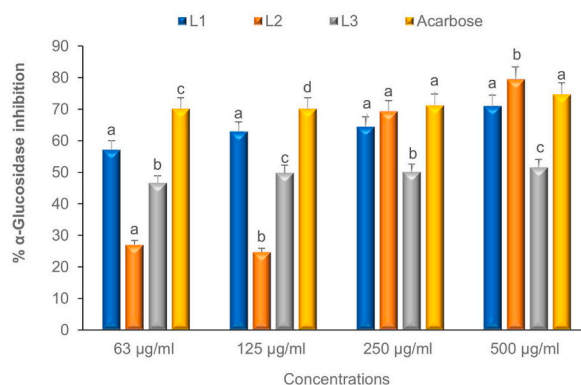
Fig. 6. Effect of L1 – L3 synthesised Schiff bases on α-glucosidase enzyme inhibition. The mean activity ± standard deviation of each compound represented by bars at each concentration with different alphabets (a–d) are significantly different at p < 0.05.

Table 4
Docked energies (kcal mol^{-1}) of compounds **L1 — L3** against selected α-amylase and α-glucosidase enzymes.

	α-Amylase	α-Glucosidase
	Binding energy (kcal mol^{-1})	
Sample L1	−9.0	−7.7
Sample L2	−8.5	−7.5
Sample L3	−8.8	−7.4
Acarbose	−7.3	−6.1

By examining the binding free energy, we gain a subtle perspective on the interplay of energy components. Notably, the energy contribution of van der Waals surpasses that of electrostatic energy in the standard reference Acarbose and compound **L1**, elucidating the predominant **effect** of van der Waals forces in shaping the overall binding energy.

3.6.2. Protein-ligand interaction after molecular dynamic simulation

The exploration of protein-ligand interactions has emerged as a pivotal approach for dissecting the intricate molecular connections that transpire within the protein's active sites when bound to ligands, as underscored by the research of Obakachi et al. [64]. A paramount aspect of this investigation is ascertaining whether the ligand or drug engages with the indispensable amino acids critical for inhibition. The nature and abundance of these interactions often wield significant influence over the resultant binding energy values when a molecule becomes intricately bound to an enzyme within a complex. In our quest to fathom the diverse array of interactions between amino acids and the ligand **L1**, alongside the reference compound Acarbose **(A.C.B.)**, we crafted a compelling depiction of protein-ligand interactions, vividly illustrated in Figs. 7and8.

Protein structures rely on a multifaceted network of non-covalent interactions, encompassing hydrophobic forces, electrostatic attractions, hydrogen bonds, and van der Waals interactions, as elucidated by Obakachi et al. in their 2021 research [64]. Notably, the interaction plot shows that the **L1** compound and the reference drug **A.C.B** both contain van der Waals interactions, which significantly contributes to protein stability. While hydrogen bonding is discernible in the case of the reference drug **A.C.B.**, it is notably absent in the L1 compound. Instead, a spectrum of other interactions, including Pi-sigma, Pi-Pi T-shaped, Pi-alkyl, and Alkyl interactions, is observed for compound **L1**. Drawing from existing literature on proteins, it's well-established that certain amino acids, namely Phe, Trp, and Tyr, often participate in π-interactions, such as π–π, cation-π, and π-alkyl bonds. The identified interactions play pivotal roles in shaping protein structure, governing protein-ligand interactions, and contributing substantively to protein stability, catalytic processes, and self-assembly dynamics [65]. Furthermore, an extensive exploration of π–π interactions' function in the interaction dynamics between aromatic drugs and proteins reveals their profound influence on drug binding to proteins, as illuminated by Shao et al. [66].

Table 5
The complex's thermodynamic binding free energy profile.

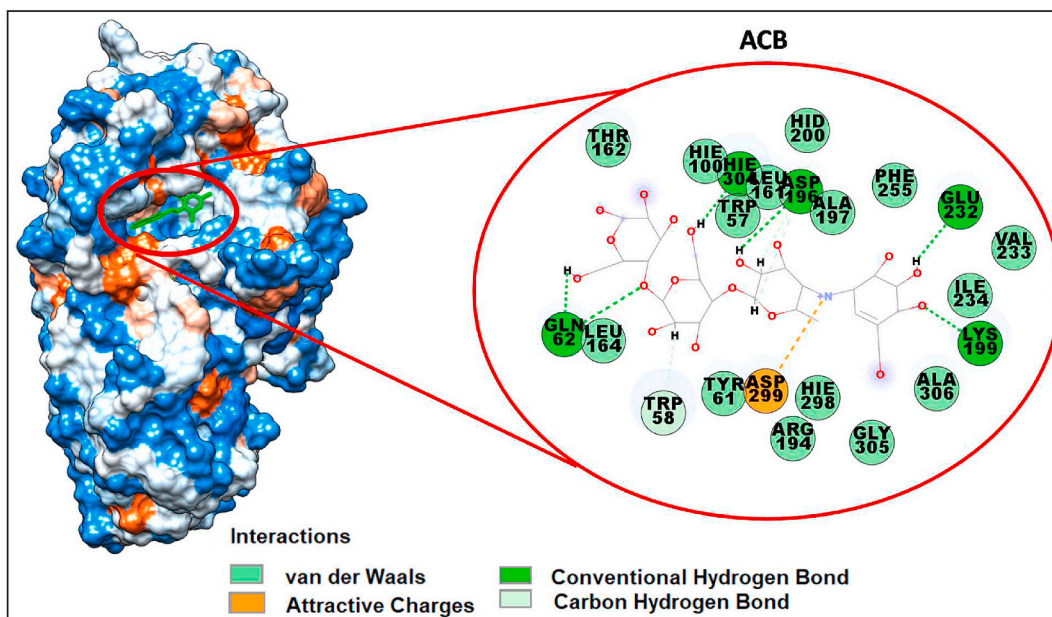| Energy Components (kcalmol^{-1})					
Complex	ΔE_{vdW}	ΔE_{elec}	ΔG_{gas}	ΔG_{solv}	ΔG_{bind}
Acarbose + α-Amylase	−54.154	15.846	−38.307	16.101	−22.206
L1 + α-Amylase	−35.064	2.939	−32.125	9.497	−22.627

Fig. 7. Interactive structures of the α-Amylase in complex with Acarbose in 3D and 2D.
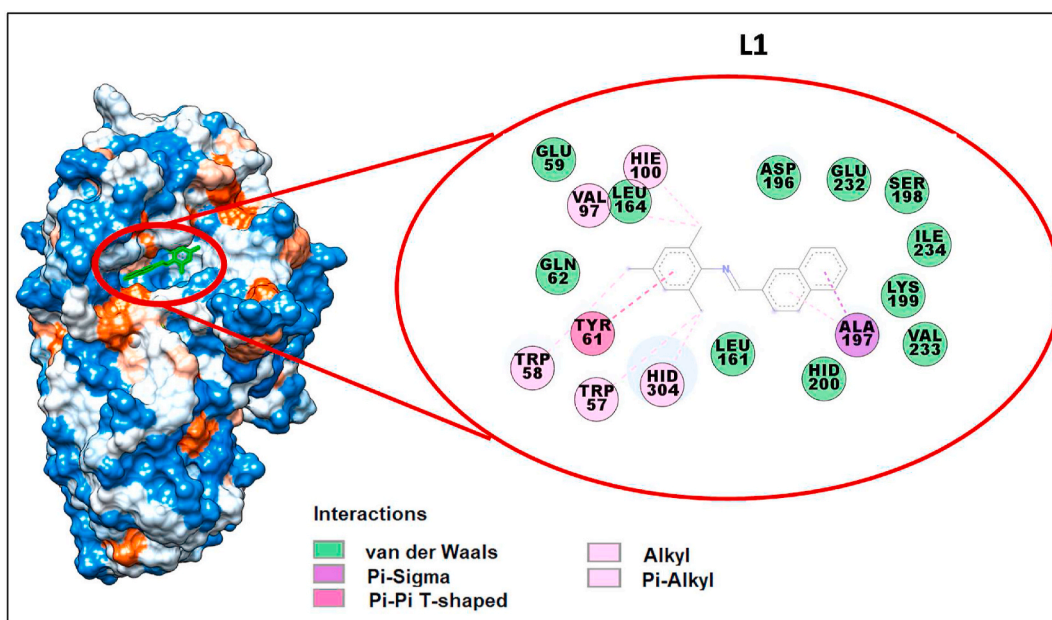

Fig. 8. Interactive structures of the α-Amylase in complex with **L1** in 3D and 2D.

3.6.3. Molecular dynamics studies of L1 and A.C.B. With α-AMYLASE protein

An in-depth molecular dynamic simulation (M.D.S.) investigation was conducted, encompassing 100 nano-second simulations. During this extensive simulation period, a meticulous analysis was undertaken, tracking and calculating critical structural parameters, including the Root Mean Square Deviation (RMSD), Radius of Gyration (RoG), and Root Mean Square Fluctuation (RMSF). These parameters were evaluated for both the ligand-bound and free (apo-enzyme) trajectories, yielding insightful data that was further visualised through plots and graphical representations.

A gauge of structural stability and system convergence is the Root Mean Square Deviation (RMSD), with lower values denoting greater stability [64]. In the context of the α-Amylase systems, including the bound **L1**, reference Acarbose **(A.C.B.)**, and unbound α-Amylase (Apo), both **L1** and **A.C.B.** converge nearly immediately, akin to the unbound system, which converges in less than 2ns (Fig. 9a). The C-alpha RMSD backbone atoms of all configurations exhibit relative stability, albeit with subtle differences. Notably, the

Apo system displays a slightly lower RMSD ($\approx$1.4 Å) than **A.C.B.**, with an RMSD of ($\approx$1.6 Å), while the **L1** bound system exhibits a higher RMSD ($\approx$1.2 Å). The average RMSD values for α-Amylase (Apo), **A.C.B.**, and **L1** are 1.235 Å, 1.285 Å, and 1.161 Å, respectively. These results highlight that the **L1** system, characterised by lower RMSD values, enhances enzyme stability to a greater extent than the reference drug, which exhibits a comparatively higher RMSD than the unbound Apo system. Notably, the plots reveal that the binding of **L1** and **A.C.B.** does not compromise protein stability or integrity of the structure. In addition to determining the RMSD, we examined the Radius of Gyration (RoG) plots for the α-Amylase protein system (Fig. 9b). RoG provides insights into structural compactness, with lower values indicating greater stability [67]. The RoG plots echo the RMSD findings, with the **L1** compound binding leading to enhanced structural compactness and heightened system stability compared to the apo-enzyme and the standard drug. The average RoG values for A.P.O., A.C.B., and **L1** are 23.204 Å, 23.143 Å, and 23.115 Å, respectively, further underscoring the stability conferred by the **L1** compound1. Furthermore, we delved into the Root Mean Square Fluctuation (RMSF) plot for the α-Amylase protein system (Fig. 9c). RMSF illuminates the impact of ligand binding on active site residue behaviour, with high RMSF values signifying greater flexibility and movement. Remarkably, the standard **A.C.B.** and the **L1** compound exhibited the maximum levels of fluctuation values, suggesting increased residue flexibility. This observation contrasts with the high RoG and RMSD values observed for the apo-enzyme and the reference compound, emphasising the multifaceted dynamics in the system.

3.6.4. Snapshot analysis of protein-ligand interactions using MD simulations

Using molecular dynamics simulations and analysing snapshots at regular intervals provide deep insights into the stability and consistency of interaction between protein and ligand [68]. These insights help researchers to understand the mechanisms of drug action better and to design more effective drugs with improved stability and efficacy. Overall, analysing the snapshots at regular intervals can provide a powerful tool for studying protein-ligand interactions and developing new drugs with improved therapeutic properties [69]. The snapshots were taken within the range of 25–100 ns at 25 ns intervals for L1 and analysed to affirm the consistencies between α-amylase-**L1** interactions (Fig. 10). The analysis showed that, most of the L1-residue interactions were stable throughout the simulation period, predicting that **L1** forms a very stable complex with the protein. This finding indicates that the protein-ligand interaction of the compound **L1** is consistent and stable over time, which is an important factor in drug design and development.

3.6.5. Principle component analysis (P.C.A.)

Several articles discuss the use of Principal Component Analysis (PCA) to elucidate MD simulations of biological macromolecules [70,71]. This analysis (PCA) provides insights into the displacement patterns of Amylase C-α atoms, a revelation unveiled through Molecular Dynamics (MD) simulations conducted using CPPTRAJ in AMBER18 GPU [72]. It was conducted to facilitate the integration of *in vitro* and computational studies of compound **L1** in relation to the reference compound acarbose. The primary objective of employing PCA was to evaluate the structural similarity or dissimilarity between the synthesised compound **L1** and the reference compound acarbose. The outcomes of the PCA analysis, as depicted in Fig. 11, revealed a notable structural resemblance between these compounds. This structural similarity observed between **L1** and acarbose is instrumental in understanding the remarkably close binding affinities observed in Table 5, which stand at −22.206 kcal/mol for acarbose and −22.627 kcal/mol for **L1**. This synergy between computational and *in vitro* findings underscores the potential of **L1** as a candidate with comparable binding affinity to acarbose, a significant result with implications for further drug development and therapeutic applications. Furthermore, the PCA
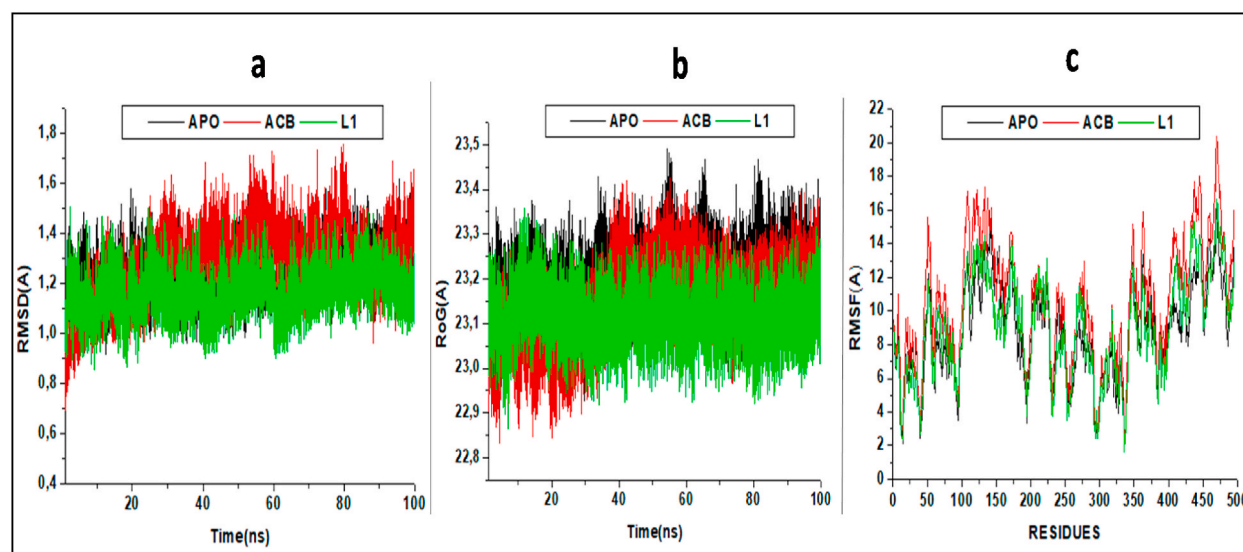

Fig. 9. showcases (a) RMSD, (b) RoG, and (c) RMSF plots in comparison for α-Amylase systems (A.P.O., A.C.B., and L1) during 100 ns MD simulations.
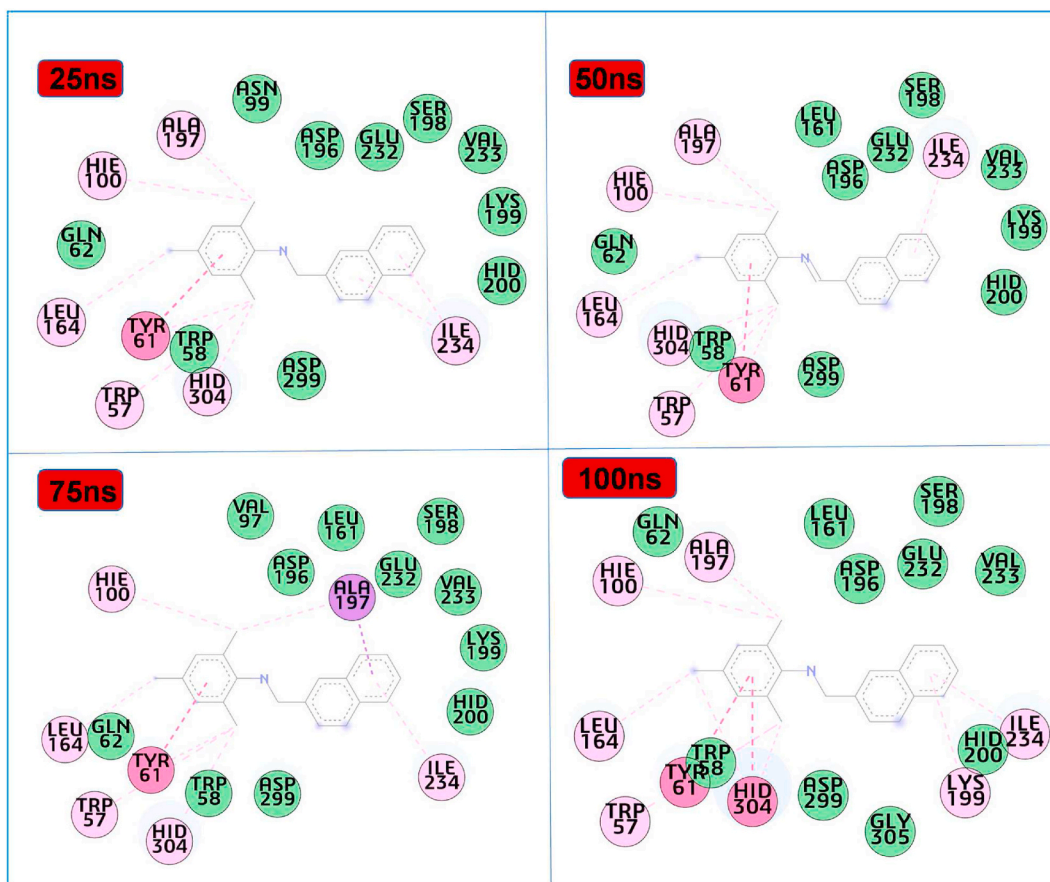
Fig. 10. Snapshot Images captured at 25 ns, 50 ns, 75 ns, and 100 ns intervals, depicting essential site residues and their interactions with L1 within the active pocket of α-amylase.

analysis of Amylase protein dynamics during interactions with inhibitors, specifically PC1 and PC2 components, unveiled key attributes of magnitude. It clarified the patterns of atomic displacements, showcasing their unidirectional and uniquely oriented nature, which can be attributed to distinct vibrational modes. The PCA scatter plot in Fig. 11 visually represents the unbound Amylase, Amylase-ACB complex, and Amylase-L1 complex.
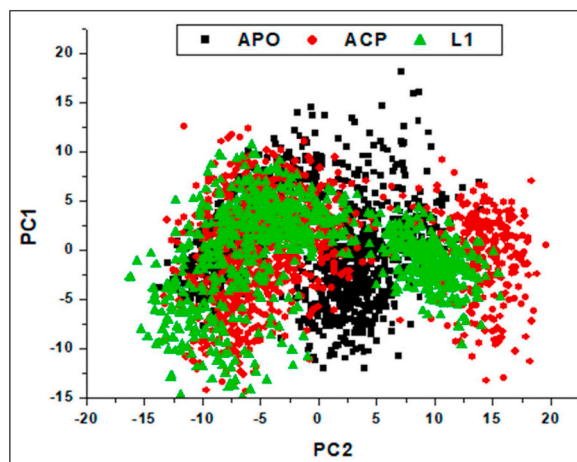

Fig. 11. Illustration of the Principal Component Analysis (PCA) of C-α backbone atoms, tracking Apo Amylase, L1, and A.C.B. bound Amylase conformations across the trajectories PC1 and PC2 throughout the 100 ns MD simulation.

The plot depicted unique conformations and movements within the critical subspace defined by the two principal components. While the Apo system exhibited inter-residue displacement along the eigenvectors, the bound systems demonstrated pronounced separation in motion patterns between the **A.C.B.** and **L1** complex systems. The α-amylase-**L1** complex displayed a dispersed good motion along the two eigenvectors, similar to the α-amylase-ACB complex. The binding of **L1** molecules to the Amylase enzyme could potentially lead to increased structural activity similar to the compact motions exhibited by the A.C.B. molecule. These findings align with the earlier discussed results, collectively supporting the notion that the binding of the proposed molecules stabilised a highly active conformation that promotes α-amylase enzymatic activity inhibition.

The results from the *in silico* studies (molecular docking, molecular dynamic simulation and PCA) indicated that **L1** bound to the same pocket as acarbose and had very close binding affinities. Hence, the need to carry out kinetic studies in future experiments before we could conclude if they both have the same mode of inhibition (competitive or non-competitive inhibition). Knowing these will enhance our understanding of how they could constitute a better alternative to acarbose. Should it be discovered subsequently that this compound could bind to other allosteric sites on the enzyme, they could be modified chemically to possibly display lesser adverse effects compared to acarbose without compromising their excellent antidiabetic activity.

3.7. In vitro antioxidant properties of L1 – L3

3.7.1. Nitric oxide (NO) scavenging activity

Fig. 12 displays the NO scavenging effects of the compounds. At 63–250 μg/mL, sample **L1** activities were significantly higher than those of the other compounds investigated and Trolox. Although sample **L2** activity at 500 μg/mL was lower compared with the other test compounds and standard, the 70.91 μg/mL and 91.21 μg/mL IC_{50} values (Table 6) respectively indicates sample **L1** and **L3** have better NO scavenging antioxidant potency compared with Trolox (IC_{50} = 109.59 μg/mL).

3.7.2. DPPH radical mopping activity

The amount to which **L1 - L3** could donate and pair with the odd electrons in the DPPH free radical is shown by the data in Fig. 13. **L1 - L3** antioxidant capacities at the test concentrations were significantly lower than those of Trolox (IC_{50} = 13.62 μg/mL) despite the fact that at 500 μg/mL, the compound's DPPH scavenging capabilities were statistically equivalent. Sample **L1** has the least IC_{50} value of 25.44 μg/mL. It has the most superior Trolox equivalent antioxidant capacity (TACE) value, followed by **L2** and **L3**, respectively (Table 6). Using quantum chemical descriptor values, particularly E_{HOMO} and ionization potential, it is possible to explain further why **L1** has better antioxidant activity than **L2** and **L3**. These two variables express how well a substance can donate electrons. The ability to donate electrons declines with decreasing E_{HOMO} (and increases with increasing ionization potential). Thus, **L1**, which had a greater E_{HOMO} and a lower ionization potential than the other compounds, produced the best DPPH radical scavenging ability, making it a better choice for developing therapeutic antioxidants [73].

3.7.3. Ferric reducing power of L1 – L3

The result in Fig. 14 compares the reducing power of the synthesised Schiff bases with Trolox at different concentrations. At 63–250 μg/mL, Fe^{3+} reduction properties of the compounds were significantly lower than those of the standard antioxidant. However, at these concentrations, the F.R.P. of the compounds were not statistically different from each other. Although samples L1 and L2 showed slightly better abilities at 500 μg/mL, the 292.51 μg/mL IC_{50} of Trolox in Table 6 indicates its superior potency relative to the synthesised compounds.

3.8. Druglikeness and pharmacokinetics properties of L1 – L3

Compounds **L1 – L3** displayed promising antidiabetes and antioxidant properties. Therefore, the need to predict their drug-likeness properties using appropriate web tools. SwissADME and pKCMS are web-based analytical tools used to approximate the drug-like nature, ADME parameters, pharmacokinetic properties and toxicity of potential drug candidates [74,75]. The physicochemical and pharmacokinetic parameters of **L1 – L3** are given in Table 7 and related with the acceptable threshold of Lipinski's Ro5. Reports indicate that promising drug molecules should comply with the acceptable threshold of Lipinski's Ro5 by not exceeding it or perhaps have a minimal violation [76]. We predicted physicochemical properties such as molecular weight (M.W.), aqueous solubility (Log S), lipophilicity (Log P), hydrogen bond donor (HBD), and acceptor (H.B.A.) ability, rotatable bonds (RotB), topological polar surface area (TPSA), and skin permeation (LogKp). We also estimated the toxicity and the pharmacokinetic parameters which include P-glyco-protein (P-gp) substrate, blood-brain barrier (BBB) permeant and gastrointestinal (GI) absorption.

Molecular weight of the compounds does not violate Lipinski's Ro5, which ascribes 500 g/mol as the M.W. of a promising drug molecule. Drug molecules with M.W. within the threshold of Lipinski's Ro5 find it easier to be transported to biomolecules target [77]. The LogS value of **L1** and **L2** fell within the range of acceptable standard of $0 \rightarrow -6$ mol/L while **L3** deviates minimally. These depict that, **L1** and **L2** can easily permeate through the intestinal epithelium surface because they are lipophilic in nature. The predicted LogP values for **L2** and **L3** have minimal violation for Lipinski's Ro5 (<5) while **L1** falls under the acceptable range. We could deduce that **L1** is more lipophilic than **L2** and **L3**, perhaps the reason why it displayed better antidiabetes potential relative to other compounds and even reference drug. The predicted values for TPSA are within the accepted values of (≤140) for **L1 – L3**. This implies that the compounds could be transported through a lipid bilayer that is densely packed, i.e., the gastrointestinal tract (G.T.) [78]. Drugs with small TPSA values tend to penetrate through the cells easily when compared with the ones having high values and this validates their bioavailability together with using them as therapeutics in the future. RotBs, HBDs, and HBAs also pinpoint the tendency of the
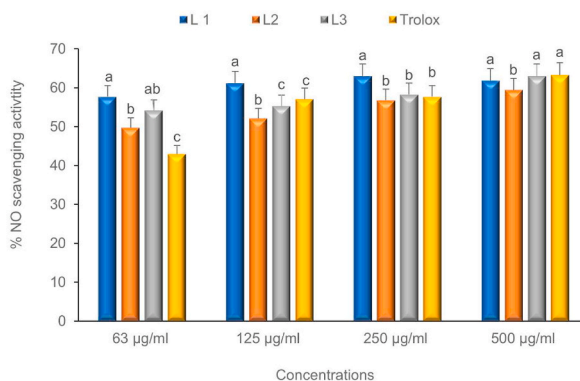
Fig. 12. L1 – L3 synthesised Schiff bases NO• radical scavenging activtities compared with Trolox at increasing concentration. The mean activity ± standard deviation of each compound represented by bars at each concentration with different alphabets (a–c) are significantly different at p < 0.05.

Table 6
Antioxidant potentials of **L1** – **L3** Schiff bases *in vitro*.

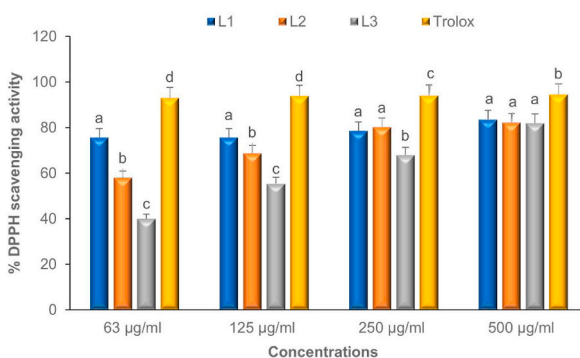| Compounds	FRAP (µg/mL)	DPPH (µg/mL)	NO (µg/mL)
L1	>500	25,44	70,91
L2	>500	35,69	119,68
L3	>500	67,81	91,21
Acarbose (Standard)	292,51	13,62	109,59

Fig. 13. L1 – L3 synthesised Schiff bases DPPH radical scavenging activities compared with Trolox at increasing concentration. The mean activity ± standard deviation of each compound represented by bars at each concentration with different alphabets (a–c) are significantly different at p < 0.05.

compounds to be promising drug candidates. Rotatable bonds could be defined as typical single bonds, joined to a nonterminal heavy atom and not present in the ring [79]. They reveal the molecular flexibility of drug compounds. In Table 7, the estimated values for RotBs, HBD.s, and H.B.A.s fell within the acceptable threshold of Lipinski's Ro5.

Intestinal absorption is one of the critical stages that is very crucial in the discovery of orally bioavailable drugs [80]. In the intestine, a promising drug candidate should be absorbed easily. All the compounds displayed high GI absorption except **L3**, and only **L1** has the tendency to penetrate through the brain-blood barrier (BBB). P-glycoprotein in the intestine reduces the bioavailability of a wide range of drugs [81]. **L1** and **L2** are not P-gp substrates, while **L3** does, and this indicates their promising bioavailability. The rate at which the compounds penetrate through the skin is in the order of **L3** > **L2** > **L1**.

4. Conclusion

Three Schiff bases were synthesised from 2-naphthaldehyde and aromatic amines and subsequently characterized using UV–vis, FT-IR, and NMR spectroscopic techniques. X-ray structural analysis of compounds **L2** and **L3** revealed that the naphthalene ring in both molecules is almost coplanar with the imine functional group, as shown by their torsion angles. Notably, the crystal packing of **L2** and **L3** displayed prominent C–H … π interactions. Among various intermolecular contacts, H⋯H interactions were found to contribute significantly to the Hirshfeld surfaces of both compounds. Calculated quantum chemical parameters provided insights into their
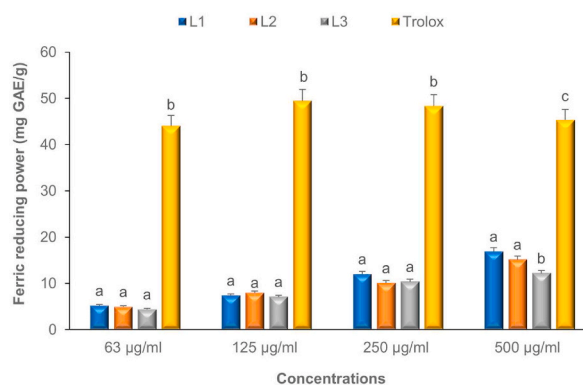
Fig. 14. L1 – L3 synthesised Schiff bases Fe^{3+} reducing power activities compared with Trolox at increasing concentration. The mean activity $\pm$ standard deviation of each compound represented by bars at each concentration with different alphabets (a–c) are significantly different at $p < 0.05$.

Table 7
Estimated pharmacokinetics and physicochemical parameters of **L1** – **L3**.

	L1	L2	L3	Acceptable threshold (Ro5)
Physicochemical properties				
Molecular weight (Da)	259.34	273.37	315.45	<500Da
Log*P*	4.83	5.16	6.02	<5
LogS (mol/L)	−5.18	−5.48	−6.26	$0 \to -6$
TPSA (A^2)	12.36	12.36	12.36	≤140
HBA	1	1	1	≤10
HBD	0	0	0	≤5
RotBs	2	2	4	<10
Pharmacokinetics properties				
G.I. absorption	High	High	Low	
B.B.B. Permeant	Yes	No	No	
P-gp Substrate	No	No	Yes	
LogKp (skin permeation)	−4.19	−4.01	−3.45	

chemical reactivity and stability, with the order being **L1** > **L3** > **L2**. *In vitro* antidiabetes indicated that **L1** exhibited superior activity compared to its counterparts and even outperformed the acarbose. Computational investigations such as molecular docking, MD simulation, post-MD and PCA were conducted to corroborate the favourable *in vitro* results of **L1's** efficacy. The binding score and binding energies of **L1** outshined the one for acarbose (reference drug). The RMSD, RMSF and RoG results from post-MD analysis predicted that, L1 will actively bind the targets and significantly impose structural stability on α-amylase relative to acarbose. The outcome of the PCA analysis revealed a structural resemblance between **L1** and acarbose. The convergence and consistency in all the computational parameters substantiate the reliability of L1's interaction with α-amylase protein, aligning with its potent *in vitro* activity. Furthermore, **L1** – **L3** demonstrated moderate to good antioxidant properties, with both **L1** and **L3** displaying better NO free radical scavenging activities than **L2** and the reference drug. Remarkably, all these compounds exhibited minimal violations of Lipinski's Rule of Five (Ro5), suggesting their potential as orally less toxic and bioavailable templates for the design of antidiabetic therapeutic agents.

CRediT authorship contribution statement

Segun D. Oladipo: Writing - review & editing, Writing - original draft, Visualization, Resources, Methodology, Funding acquisition, Formal analysis, Data curation, Conceptualization. **Robert C. Luckay:** Writing - review & editing, Writing - original draft, Visualization, Validation, Supervision, Resources, Project administration, Funding acquisition, Conceptualization. **Kolawole A. Olofinsan:** Writing - review & editing, Writing - original draft, Software, Methodology, Formal analysis, Data curation. **Vincent A. Obakachi:** Writing - review & editing, Writing - original draft, Software, Methodology, Data curation. **Sizwe J. Zamisa:** Writing - review & editing, Writing - original draft, Software, Methodology, Formal analysis, Data curation. **Adesola A. Adeleke:** Writing - review & editing, Software, Resources, Methodology, Formal analysis, Data curation. **Abosede A. Badeji:** Writing - review & editing, Software, Methodology, Formal analysis, Data curation. **Segun A. Ogundare:** Writing - review & editing, Formal analysis, Data curation. **Blassan P. George:** Writing - review & editing, Methodology, Formal analysis.

Declaration of competing interest

The authors declare that they have no known competing financial interests or personal relationships that could have appeared to

influence the work reported in this paper.

Acknowledgment

Appendix A. Supplementary data

Supplementary data to this article can be found online at https://doi.org/10.1016/j.heliyon.2023.e23174.

References

[1] E.S. Ford, C. Li, G. Zhao, Prevalence and correlates of metabolic syndrome based on a harmonious definition among adults in the U.S, J. Diabetes 2 (2010) 180–193.
[2] B. Deepthi, K. Sowjanya, B. Lidiya, R.S. Bhargavi, P.S. Babu, A modern review of diabetes mellitus: an annihilatory metabolic disorder, J. In Silico In Vitro Pharmacol 3 (2017) 1.
[3] A.M. Ahmed, History of diabetes mellitus, Saudi Med. J. 23 (2002) 373–378.
[4] E.J. Prpa, B.H. Bajka, P.R. Ellis, P.J. Butterworth, C.P. Corpe, W.L. Hall, A systematic review of in vitro studies evaluating the inhibitory effects of polyphenol-rich fruit extracts on carbohydrate digestive enzymes activity: a focus on culinary fruits consumed in Europe, Crit. Rev. Food Sci. Nutr. 61 (2021) 3783–3803.
[5] H.O. Omoregie, T.L. Yusuf, S.D. Oladipo, K.A. Olofinsan, M.B. Kassim, S. Yousuf, Antidiabetes, antimicrobial and antioxidant studies of mixed β-diketone and diimine copper (II) complexes, Polyhedron 217 (2022), 115738.
[6] M. Zhang, R. Feng, M. Yang, C. Qian, Z. Wang, W. Liu, J. Ma, Effects of metformin, Acarbose, and sitagliptin monotherapy on gut microbiota in Zucker diabetic fatty rats, B.M.J. Open Diabetes Res. Care 7 (2019), e000717.
[7] H. Bishoff, Pharmacological properties of the novel glucosidase inhibitors BAY m 1099 (miglitol) and BAY o 1248, Diabetes Res. Clin. Pract. 1 (1985) S53.
[8] M.S. Brewer, Natural antioxidants: sources, compounds, mechanisms of action, and potential applications, Compr. Rev. Food Sci. Food Saf. 4 (2011) 221–247.
[9] H. Sies, Oxidative stress: oxidants and antioxidants, Exp. Physiol. 82 (1997) 291–295.
[10] S.D. Oladipo, B. Omondi, C. Mocktar, Co (III) N, N'-diarylformamidine dithiocarbamate complexes: synthesis, characterisation, crystal structures and biological studies, Appl. Organomet. Chem. 34 (2020), e5610.
[11] I. Kostova, L. Saso, Advances in research of Schiff-base metal complexes as potent antioxidants, Curr. Med. Chem. 20 (2013) 4609–4632.
[12] M. Valko, C.J.B. Rhodes, J. Moncol, M.M. Izakovic, M. Mazur, Free radicals, metals and antioxidants in oxidative stress-induced cancer, Chem. Biol. Interact. 160 (2006) 1–40.
[13] B. Halliwell, Antioxidants in human health and disease, Annu. Rev. Nutr. 16 (1996) 33–50.
[14] T.L. Yusuf, S.D. Oladipo, S.A. Olagboye, S.J. Zamisa, G.F. Tolufashe, Solvent-free synthesis of nitrobenzyl Schiff bases: characterisation, antibacterial studies, density functional theory and molecular docking studies, J. Mol. Struct. 1222 (2020), 128857.
[15] J. Ceramella, D. Iacopetta, A. Catalano, F. Cirillo, R. Lappano, M.S. Sinicropi, A review on the antimicrobial activity of schiff bases: data collection and recent studies, Antibiotics 11 (2022) 191.
[16] A.A. Adeleke, S.J. Zamisa, B. Omondi, Ag(I) complexes of imine derivatives of unexpected 2-thiophenemethylamine homo-coupling and bis-(E)-N-(furan-2-ylmethyl)-1-(quinolin-2-yl)methanimine, Molbank 2021 (2) (2021) M1235.
[17] T.L. Yusuf, D.C. Akintayo, S.D. Oladipo, A.A. Adeleke, K. Olofisan, B. Vatsha, N. Mabuba, The effect of structural configuration on the D.N.A. binding and in vitro antioxidant properties of new copper (ii) N₂O₂ Schiff base complexes, New J. Chem. 46 (2022) 12968–12980.
[18] S.R. Prasad, N.D. Satyanarayan, A.S.K. Shetty, B. Thippeswamy, B. Thippeswamy, Synthesis, antimicrobial, and antitubercular evaluation of new Schiff bases with in silico ADMET and molecular docking studies, Eur. J. Chem. 13 (2022) 109–116.
[19] H.R. Afzal, N.U.H. Khan, K. Sultana, A. Mobashar, A. Lareb, A. Khan, A. Gull, H. Afzaal, M.T. Khan, M. Rizwan, M. Imran, Schiff bases of pioglitazone provide better antidiabetic and potent antioxidant effect in a streptozotocin–nicotinamide-induced diabetic rodent model, ACS Omega 6 (2021) 4470–4479.
[20] G. Matela, Schiff bases and complexes: a review on anti-cancer activity, Anti Cancer Agents Med. Chem. 20 (2020) 1908–1917.
[21] A. Hameed, M. Al-Rashida, M. Uroos, S. Abid Ali, K.M. Khan, Schiff bases in medicinal chemistry: a patent review (2010-2015), Expert Opin. Ther. Pat. 27 (2017) 63–79.
[22] S.A. Olagboye, T.L. Yusuf, S.D. Oladipo, S.J. Zamisa, Crystal structure of bis (2-hydroxy-6-((phenylimino) methyl) phenolato-κ2N, O) copper (II), C₂₆H₂₀CuN₂O₄, Z. fur. Krist – New Cryst. 235 (2020) 689–692.
[23] S.D. Oladipo, T.L. Yusuf, S.J. Zamisa, G.F. Tolufashe, K.A. Olofinsan, Z. Tywabi-Ngeva, N. Mabuba, Synthesis, crystal structure with free radical scavenging activity and theoretical studies of Schiff bases derived from 1-naphthylamine, 2, 6-diisopropylaniline, and substituted benzaldehyde, Eur. J. Chem. 12 (2021) 204–215.
[24] A.A. Adesola, S.J. Zamisa, B. Omondi, Crystal structure of 4-(1-phenylimidazo[1,5-a]pyridin-3-yl)benzoic acid (C₂₀H₁₄N₂O₂), Z. fur Krist. - New Cryst. Struct. 234 (2019) 1157–1159.
[25] Bruker APEX II, Bruker AXS: Madison, Wisconsin, USA, 2009.
[26] Bruker SAINT, Bruker AXS: Madison, Wisconsin, USA, 2009.
[27] Bruker SADABS, Bruker AXS: Madison, Wisconsin, USA, 2009.
[28] G.M. Sheldrick, A short history of Shelx, Acta Crystallogr., Sect. A: Found. Crystallogr. 64 (2008) 112–122.
[29] O.V. Dolomanov, L.J. Bourhis, R.J. Gildea, J.A. Howard, H. Puschmann, OLEX2: a complete structure solution, refinement and analysis program, J. Appl. Crystallogr. 42 (2009) 339–341.
[30] O.B. Ibitoye, K. Olofinsan, K. Teralı, U.M. Ghali, T.O. Ajiboye, Bioactivity-guided isolation of antidiabetic principles from the methanolic leaf extract of Bryophyllum pinnatum, J. Food Biochem. 42 (2018), e12627.
[31] K.A. Olofinsan, O.L. Erukainure, B.K. Brian, M.S. Islam, Harpephyllum caffrum stimulates glucose uptake, abates redox imbalance and modulates purinergic and glucogenic enzyme activities in oxidative hepatic injury, Asian Pac. J. Trop. Biomed. 12 (2022) 9.
[32] G.A. Kurian, S. Suryanarayanan, A. Raman, J. Padikkala, Antioxidant effects of ethyl acetate extract of Desmodium gangeticum root on myocardial ischemia reperfusion injury in rat hearts, Chin. Med. 5 (2010) 1–7.
[33] A. Turkoglu, M.E. Duru, N. Mercan, I. Kivrak, K. Gezer, Antioxidant and antimicrobial activities of Laetiporus sulphureus, Bull.) Murrill. Food Chem. 101 (2007) 267–273.

[34] Y.P. Tan, E.W.C. Chan, Antioxidant, antityrosinase and antibacterial properties of fresh and processed leaves of Anacardium occidentale and Piper betle, Food Biosci. 6 (2014) 17–23.

[35] A.D. Becke, Density-functional thermochemistry. I. The effect of the exchange-only gradient correction, J. Chem. Phys. 96 (1992) 2155–2160.

[36] J. Martínez, Local reactivity descriptors from degenerate frontier molecular orbitals, Chem. Phys. Lett. 478 (2009) 310–322.

[37] V. Nahoum, G. Roux, V. Anton, P. Rouge, A. Puigserver, H. Bischoff, B. Henrissat, F. Payan, Crystal structures of human pancreatic α-amylase in complex with carbohydrate and proteinaceous inhibitors, Biochem. J. 346 (2000) 201–208.

[38] F. Cardona, C. Parmeggiani, E. Faggi, C. Bonaccini, P. Gratteri, L. Sim, T.M. Gloster, S. Roberts, G.J. Davies, D.R. Rose, A. Goti, Total syntheses of casuarine and its 6-O-α-glucoside: complementary inhibition towards glycoside hydrolases of the GH31 and GH37 families, Chem. Eur J. 15 (2009) 1627–1636.

[39] J. Wang, W. Wang, P.A. Kollman, D.A. Case, Automatic atom type and bond type perception in molecular mechanical calculations, J. Mol. Graph. Model. 25 (2006) 247–260.

[40] M.D. Hanwell, D.E. Curtis, D.C. Lonie, T. Vandermeersch, E. Zurek, G.R. Hutchison, Avogadro: an advanced semantic chemical editor, visualisation, and analysis platform, J. Cheminf. 4 (2012) 1–17.

[41] D. Systèmes, Biovia, Discovery Studio Modeling Environment, Dassault Systèmes Biovia, San Diego, CA, USA, 2016.

[42] P.C. Nair, J.O. Miners, Molecular dynamics simulations: from structure function relationships to drug discovery, silico Pharmacol 2 (2014) 1–4.

[43] J.P. Ryckaert, G. Ciccotti, H.J. Berendsen, Numerical integration of the cartesian equations of motion of a system with constraints: molecular dynamics of n-alkanes, J. Comput. Phys. 23 (1977) 327–341.

[44] H.J. Berendsen, J.V. Postma, W.F. Van Gunsteren, A.R.H.J. DiNola, J.R. Haak, Molecular dynamics with coupling to an external bath, J. Chem. Phys. 81 (1984) 3684–3690.

[45] P. Gonnet, P.- Shake, A quadratically convergent SHAKE in O (n2), J. Comp. Physiol. 220 (2007) 740–750.

[46] S. Le Grand, A.W. Götz, R.C. Walker, SPFP: speed without compromise—a mixed precision model for GPU accelerated molecular dynamics simulations, Comput. Phys. Commun. 184 (2013) 374–380.

[47] L. Larini, R. Mannella, D. Leporini, Langevin stabilisation of molecular-dynamics simulations of polymers by means of quasisymplectic algorithms, J. Chem. Phys. 126 (2007), 104101.

[48] M. Ylilauri, O.T. Pentikäinen, MMGBSA as a tool to understand the binding affinities of filamin–peptide interactions, J. Chem. Inf. Model. 53 (2013) 2626–2633.

[49] D.R. Roe, T.E. Cheatham III, PTRAJ and CPPTRAJ: software for processing and analysis of molecular dynamics trajectory data, J. Chem. Theor. Comput. 9 (2013) 3084–3095.

[50] E. Seifert, OriginPro 9.1: scientific data analysis and graphing software-software review, J. Chem. Inf. Model. 54 (2014) 1552.

[51] S.D. Oladipo, T.L. Yusuf, S.J. Zamisa, M. Shapi, T.J. Ajayi, Synthesis, crystal structure, Hirshfeld surface analysis and DFT studies of N-(2, 6-diisopropylphenyl)-1-(4-methoxyphenyl) methanimine, J. Mol. Struct. 1241 (2021), 130620.

[52] W. Kemp, Organic Spectroscopy, Bloomsbury Publishing, 2017.

[53] G.M. Ferrence, C.A. Tovee, S.J. Holgate, N.T. Johnson, M.P. Lightfoot, K.L. Ward, S.C. Nowakowska-Orzechowska, C.S.D. Communications of the Cambridge structural database, IUCrJ 10 (2023) 6–15.

[54] F.N. Moghadam, M. Amirnasr, K. Eskandari, S. Meghdadi, A new disulfide Schiff base as a versatile "OFF–ON–OFF" fluorescent–colorimetric chemosensor for sequential detection of C.N.⁻ and Fe³⁺ ions: combined experimental and theoretical studies, New J. Chem. 43 (2019) 13536–13544.

[55] G. Orona, V. Molinar, F.R. Fronczek, R. Isovitsch, 2-[(Naphthalen-1-ylmethylidene) amino]-5-methylphenol, Acta Crystallogr. E 67 (2011) o2505–o2506.

[56] M.A. Spackman, D. Jayatilaka, Hirshfeld surface analysis, CrystEngComm 11 (2009) 19–32.

[57] P.R. Spackman, M.J. Turner, J.J. McKinnon, S.K. Wolff, D.J. Grimwood, D. Jayatilaka, M.A. Spackman, CrystalExplorer: a program for Hirshfeld surface analysis, visualisation and quantitative analysis of molecular crystals, J. Appl. Crystallogr. 54 (2021) 1006–1011.

[58] M.A. Spackman, P.G. Byrom, A novel definition of a molecule in a crystal, Chem. Phys. Lett. 267 (1997) 215–220.

[59] R.K. Mudsainiyan, S.K. Pandey, A combined theoretical calculation and Hirshfeld surface analysis of cooperative non-covalent interactions in the crystal packing in [Cu (L1) 2 (E.D.A.)], Z. Anorg. Allg. Chem. 643 (2017) 1245–1252.

[60] S.D. Oladipo, S.J. Zamisa, A.A. Badeji, M.A. Ejalonibu, I.A. Lawal, A. Henni, M.M. Lawal, Ni²⁺ and Cu²⁺ complexes of N-(2,6-dichlorophenyl)-N-mesityl formamidine dithiocarbamate structural and functional properties of CYP3A4, Sci. Rep. 13 (2023), 13414.

[61] E.D. Akpan, S.D. Oladipo, T.W. Quadri, L.O. Olasunkanmi, E.E. Nwanna, B. Omondi, E.E. Ebenso, Formamidine-based thiuram disulfides as efficient inhibitors of acid corrosion of mild steel; electrochemical, surface and density functional theory/Monte Carlo simulation studies, ACS Omega 7 (2022) 26076–26091.

[62] M.C. Hernández-Rodríguez, M. Rosales-Hernández, J. E Mendieta-Wejebe, M. Martinez-Archundia, J. Correa Basurto, Current tools and methods in molecular dynamics (M.D.) simulations for drug design, Curr. Med. Chem. 23 (2016) 3909–3924.

[63] C. Wang, D.A. Greene, L. Xiao, R. Qi, R. Luo, Recent developments and applications of the MMPBSA method, Front. Mol. Biosci. 4 (2018) 87.

[64] V.A. Obakachi, N.D. Kushwaha, B. Kushwaha, M.C. Mahlalela, S.R. Shinde, I. Kehinde, R. Karpoormath, Design and synthesis of pyrazolone-based compounds as potent blockers of SARS-CoV-2 viral entry into the host cells, J. Mol. Struct. 1241 (2021), 130665.

[65] S.K. Burley, G.A. Petsko, Aromatic-aromatic interaction: a mechanism of protein structure stabilisation, Science 229 (1985) 23–28.

[66] J. Shao, B.P. Kuiper, A.M.W. Thunnissen, R.H. Cool, L. Zhou, C. Huang, B.W. Dijkstra, J. Broos, The role of tryptophan in π interactions in proteins: an experimental approach, J. Am. Chem. Soc. 144 (2022) 13815–13822.

[67] O.I. Akinpelu, M.M. Lawal, H.M. Kumalo, N.N. Mhlongo, Computational studies of the properties and activities of selected trisubstituted benzimidazoles as potential antitubercular drugs inhibiting MTB-FtsZ polymerisation, J. Biomol. Struct. Dyn. 40 (2022) 1558–1570.

[68] S.E. Nichols, R. Baron, A. Ivetac, J.A. McCammon, Predictive power of molecular dynamics receptor structures in virtual screening, J. Chem. Inf. Model. 6 (2011) 1439–1446.

[69] S.A. Hollingsworth, R.O. Dror, Molecular dynamics simulation for all, Neuron 99 (2018) 1129–1143.

[70] J. Palma, G. Pierdominici-Sottile, On the uses of PCA to characterise molecular dynamics simulations of biological macromolecules: basics and tips for an effective use, ChemPhysChem 24 (2023), e202200491.

[71] A.T. Adewumi, W.M. Oluyemi, Y.A. Adekunle, N. Adewumi, M.I. Alahmdi, M.E. Soliman, N.E. Abo-Dya, Propitious indazole compounds as β-ketoacyl-ACP synthase inhibitors and mechanisms unfolded for TB cure: integrated rational design and MD simulations, ChemistrySelect 8 (2023), e202203877.

[72] R. Galindo-Murillo, D.R. Roe, T.E. Cheatham III, Convergence and reproducibility in molecular dynamics simulations of the DNA duplex d (GCACGAACGAACGAACGC), Biochim. Biophys. Acta Gen. Subj. 5 (2015) 1041–1058.

[73] S.D. Oladipo, G.F. Tolufashe, C. Mocktar, B. Omondi, Ag (I) symmetrical N, N′-diarylformamidine dithiocarbamate PPh3 complexes: synthesis, structural characterization, quantum chemical calculations and in vitro biological studies, Inorganica. Chim. Acta. 520 (2021), 120316.

[74] A. Daina, O. Michielin, V. Zoete, SwissADME: a free web tool to evaluate pharmacokinetics, drug-likeness and medicinal chemistry friendliness of small molecules, Sci. Rep. 7 (2017), 42717.

[75] D.E. Pires, T.L. Blundell, D.B. Ascher, pkCSM: predicting small-molecule pharmacokinetic and toxicity properties using graph-based signatures, J. Med. Chem. 58 (2015) 4066–4072.

[76] S.D. Oladipo, F.A. Olotu, C. Mocktar, B. Omondi, Formamidine-based thiuram disulfides: synthesis, structural characterisation, biological studies, and preliminary cheminformatics evaluation, J. Mol. Struct. 1219 (2020), 128553.

[77] F.A. Olotu, G. Munsamy, M.E. Soliman, Does size really matter? Probing the efficacy of structural reduction in the optimisation of bioderived compounds–a computational "proof-of-concept", Comput. Struct. Biotechnol. J. 16 (2018) 573–586.

[78] S. Shityakov, W. Neuhaus, T. Dandekar, C. Förster, Analysing molecular polar surface descriptors to predict blood-brain barrier permeation, Int. J. Comput. Biol. Drug Des. 6 (2013) 146–156.

[79] D.F. Veber, S.R. Johnson, H.-Y. Cheng, B.R. Smith, K.W. Ward, K.D. Kopple, Molecular properties that influence the oral bioavailability of drug candidates, J. Med. Chem. 45 (2002) 2615–2623.

[80] E. Sjögren, J. Westergren, I. Grant, G. Hanisch, L. Lindfors, H. Lennernäs, B. Abrahamsson, C. Tannergren, In silico predictions of gastrointestinal drug absorption in pharmaceutical product development: application of the mechanistic absorption model GI-Sim, Eur. J. Pharmaceut. Sci. 49 (2013) 679–698.

[81] G. Cornaire, J. Woodley, P. Hermann, A. Cloarec, C. Arellano, G. Houin, Impact of excipients on the absorption of P-glycoprotein substrates in vitro and in vivo, Int. J. Pham. 278 (2004) 119–131.